Development of time-domain differential Raman for transient thermal probing of materials

Shen Xu,[1,4] Tianyu Wang,[1,4] David Hurley,[2,5] Yanan Yue,[3] and Xinwei Wang[1,6]

[1]*Department of Mechanical Engineering, Iowa State University, Ames, Iowa 50011, USA*
[2]*Idaho National Laboratory, Idaho Falls, Idaho 83415, USA*
[3]*Department of Mechanical Engineering, Wuhan University, Wuhan, Hubei, China*
[4]*These authors contribute equally.*
[5]*david.hurley@inl.gov*
[6]*xwang3@iastate.edu*

Abstract: A novel transient thermal characterization technology is developed based on the principles of transient optical heating and Raman probing: time-domain differential Raman. It employs a square-wave modulated laser of varying duty cycle to realize controlled heating and transient thermal probing. Very well defined extension of the heating time in each measurement changes the temperature evolution profile and the probed temperature field at μs resolution. Using this new technique, the transient thermal response of a tipless Si cantilever is investigated along the length direction. A physical model is developed to reconstruct the Raman spectrum considering the temperature evolution, while taking into account the temperature dependence of the Raman emission. By fitting the variation of the normalized Raman peak intensity, wavenumber, and peak area against the heating time, the thermal diffusivity is determined as 9.17×10^{-5}, 8.14×10^{-5}, and 9.51×10^{-5} m^2/s. These results agree well with the reference value of 8.66×10^{-5} m^2/s considering the 10% fitting uncertainty. The time-domain differential Raman provides a novel way to introduce transient thermal excitation of materials, probe the thermal response, and measure the thermal diffusivity, all with high accuracy.

©2015 Optical Society of America

OCIS codes: (300.6380) Spectroscopy, modulation; (300.6450) Spectroscopy, Raman; (350.5340) Photothermal effects; (120.0120) Instrumentation, measurement, and metrology.

References and links

1. T. E. Beechem and J. R. Serrane, "Raman thermometry of microdevices: comparing methods to minimize error," Spectroscopy **26**(11), 36–44 (2011).
2. Y. N. Yue and X. W. Wang, "Review on Raman-based thermal characterization and analysis," Journal of Shanghai Second Polytechnic University **28**(3), 183–191 (2011).
3. L. Song, W. J. Ma, Y. Ren, W. Y. Zhou, S. S. Xie, P. H. Tan, and L. F. Sun, "Temperature dependence of Raman spectra in single-walled carbon nanotube rings," Appl. Phys. Lett. **92**(12), 121905 (2008).
4. T. Beechem, S. Graham, S. P. Kearney, L. M. Phinney, and J. R. Serrano, "Invited article: simultaneous mapping of temperature and stress in microdevices using micro-Raman spectroscopy," Rev. Sci. Instrum. **78**(6), 061301(2007).
5. N. Lundt, S. T. Kelly, T. Rödel, B. Remez, A. M. Schwartzberg, A. Ceballos, C. Baldasseroni, P. A. F. Anastasi, M. Cox, F. Hellman, S. R. Leone, and M. K. Gilles, "High spatial resolution Raman thermometry analysis of TiO_2 microparticles," Rev. Sci. Instrum. **84**(10), 104906 (2013).
6. A. A. Balandin, S. Ghosh, W. Bao, I. Calizo, D. Teweldebrhan, F. Miao, and C. N. Lau, "Superior thermal conductivity of single-layer graphene," Nano Lett. **8**(3), 902–907 (2008).
7. S. Chen, Q. Wu, C. Mishra, J. Kang, H. Zhang, K. Cho, W. Cai, A. A. Balandin, and R. S. Ruoff, "Thermal conductivity of isotopically modified graphene," Nat. Mater. **11**(3), 203–207 (2012).
8. Q. Li, C. Liu, X. Wang, and S. Fan, "Measuring the thermal conductivity of individual carbon nanotubes by the Raman shift method," Nanotechnology **20**(14), 145702 (2009).
9. E. Chavez-Angel, J. S. Reparaz, J. Gomis-Bresco, M. R. Wagner, J. Cuffe, B. Graczykowski, A. Shchepetov, H. Jiang, M. Prunnila, J. Ahopelto, F. Alzina, and C. M. S. Torres, "Reduction of the thermal conductivity in free-standing silicon nano-membranes investigated by non-invasive Raman thermometry," Apl Mater **2**(1), 012113

#234498 - $15.00 USD Received 11 Feb 2015; revised 7 Apr 2015; accepted 8 Apr 2015; published 10 Apr 2015
© 2015 OSA

(2014).
10. Z. Yan, C. Jiang, T. R. Pope, C. F. Tsang, J. L. Stickney, P. Goli, J. Renteria, T. T. Salguero, and A. A. Balandin, "Phonon and thermal properties of exfoliated $TaSe_2$ thin films," J. Appl. Phys. **114**(20), 204301 (2013).
11. S. Sahoo, A. P. S. Gaur, M. Ahmadi, M. J. F. Guinel, and R. S. Katiyar, "Temperature-dependent Raman studies and thermal conductivity of few-layer MoS_2," J. Phys. Chem. C **117**(17), 9042–9047 (2013).
12. Y. Yue, J. Zhang, and X. Wang, "Micro/nanoscale spatial resolution temperature probing for the Interfacial Thermal Characterization of Epitaxial Graphene on 4H-SiC," Small **7**(23), 3324–3333 (2011).
13. X. Tang, S. Xu, and X. Wang, "Corrugated epitaxial graphene/SiC Interfaces: photon excitation and probing," Nanoscale **6**(15), 8822–8830 (2014).
14. X. Tang, S. Xu, J. Zhang, and X. Wang, "Five orders of magnitude reduction in energy coupling across corrugated graphene/substrate interfaces," ACS Appl. Mater. Interfaces **6**(4), 2809–2818 (2014).
15. X. Tang, S. Xu, and X. Wang, "Nanoscale probing of thermal, stress, and optical fields under near-field laser heating," PLoS ONE **8**(3), e58030 (2013).
16. X. Tang, S. Xu, and X. Wang, "Thermal probing in single microparticle and microfiber induced near-field laser focusing," Opt. Express **21**(12), 14303–14315 (2013).
17. X. Tang, Y. Yue, X. Chen, and X. Wang, "Sub-wavelength temperature probing in near-field laser heating by particles," Opt. Express **20**(13), 14152–14167 (2012).
18. Y. Yue, X. Chen, and X. Wang, "Noncontact sub-10 nm temperature measurement in near-field laser heating," ACS Nano **5**(6), 4466–4475 (2011).
19. S. Xu, X. D. Tang, Y. N. Yue, and X. W. Wang, "Sub-micron imaging of sub-surface nanocrystalline structure in silicon," J Raman Spectrosc **44**(11), 1523–1528 (2013).
20. J. Q. Guo, X. W. Wang, and T. Wang, "Thermal characterization of microscale conductive and nonconductive wires using transient electrothermal technique," J. Appl. Phys. **101**(6), 063537 (2007).
21. H. Lin, S. Xu, X. Wang, and N. Mei, "Significantly reduced thermal diffusivity of free-standing two-layer graphene in graphene foam," Nanotechnology **24**(41), 415706 (2013).
22. G. Liu, S. Xu, T. T. Cao, H. Lin, X. Tang, Y. Q. Zhang, and X. Wang, "Thermally induced increase in energy transport capacity of silkworm silks," Biopolymers **101**(10), 1029–1037 (2014).
23. Z. L. Xu, S. Xu, X. D. Tang, and X. W. Wang, "Energy transport in crystalline DNA composites," Aip Adv **4**(1), 017131 (2014).
24. D. R. Lide, *CRC Handbook of Chemistry and Physics,* Internet Version 2007, 87th edition (Taylor and Francis, 2007).
25. G. Liu, H. Lin, X. Tang, K. Bergler, and X. Wang, "Characterization of thermal transport in one-dimensional solid materials," J. Vis. Exp. (**83**): e51144 (2014).
26. P. Klar, E. Lidorikis, A. Eckmann, I. A. Verzhbitskiy, A. C. Ferrari, and C. Casiraghi, "Raman scattering efficiency of graphene," Phys. Rev. B **87**(20), 205435 (2013).
27. M. Cardona, *Light Scattering in Solids II*, Topics in Applied Physics (Springer, 1982), Vol. 50.

1. Introduction

Raman scattering is not only applicable for structural characterization of molecular configuration and conformation in chemistry, but is also suitable for measuring physical characteristics of materials, such as temperature and stress. In Raman scattering, incident photons interact with optical phonons and exchange energy with those phonons. As a result of this interaction, the emitted photons have different frequencies from the incident ones. Raman signals generally produce a Gaussian or Lorentz peak in the spectrum. The peak intensity, wavenumber (Raman shift) and linewidth (full width at half maximum, or FWHM) of the Raman signal are tightly related to phonon emission, frequency and lifetime [1, 2]. Temperature variation of the material will affect the phonon distribution and as a consequence will perturb the Raman signals. When the temperature of a detected region goes up, the emitted Raman photon wavenumber will become smaller (softening), the intensity will decrease, and the linewidth will broaden. Raman thermometry is thus a methodology for measuring the temperature distribution and thermophysical properties of analyzed systems.

Furthermore, due to its less invasive and nondestructive feature and high spatial resolution, Raman thermometry has been widely used to determine the temperature of complicated and highly compacted structures and devices [3, 4]. Song, *et al*. [3] studied the thermal stability of single-walled carbon nanotube (SWCNT) rings with the Raman shift method in the range of 80-550 K. Beechem, *et al.* [4] mapped both temperature and stress distribution simultaneously with Raman shift of functioning polysilicon microheater. Lundt,

#234498 - $15.00 USD Received 11 Feb 2015; revised 7 Apr 2015; accepted 8 Apr 2015; published 10 Apr 2015
© 2015 OSA

et al. [5] developed a micro-Raman thermometry with a spatial resolution of 280 nm by employing anatase TiO_2 microparticles.

Since the temperature of a studied system can be measured using Raman thermometry, the intrinsic thermal conductivity of the targeted material in the system can also be quantified. In popular 2D materials investigation, the thermal conductivity of a suspended thin layer of material can be determined from the correlation between input energy increase and resulting temperature increase, while the temperature rise is determined by variation in the Raman peak shift with a thermal coefficient from additional calibration. This optical based thermal properties characterization technique has become a common tool to study the thermal conductivity of Raman active 2D materials, such as graphene [6] and extended materials from graphene family [7, 8], silicon nano-membranes [9], $TaSe_2$ thin films [10], and few-layer MoS_2 [11].

Interface energy coupling also can be investigated with Raman thermometry. Yue, *et al*. [12] successfully used a combination of Raman spectroscopy and Joule heating to achieve nanoscale temperature mapping. Their approach revealed a large thermal interface resistance between graphene and SiC. To determine the temperature variation in their experiment, additional calibration of temperature coefficients of graphene and SiC were conducted from room temperature to 250°C. Tang, *et al.* improved Raman thermometry for interface energy coupling measurements by using two separated lasers: one for well-defined localized heating and one for Raman excitation and temperature probing [13, 14]. Naturally corrugated graphene on Si, SiO_2, and SiC were studied respectively. It was determined that loose contact or point contact between the grapheme layer and the substrate was the main reason for low energy coupling at the interface. In Tang's work, calibration for temperature coefficients of graphene and substrate materials was also carried out to determine the temperature during interface probing.

With the decrease of the size of micro-devices, higher resolution temperature mapping techniques are critically needed. Near-field optical techniques make possible the scanning of delicate nanostructures with subwavelength resolution. Tang's work [15–17] utilized different structures, such as silica nanoparticles and fibers, to focus the excitation laser into an extremely small size. In their work, the effect of temperature, stress and optical field on the Raman spectrum was de-conjugated. For the first time, the stress and temperature distribution was characterized successfully with 20 nm resolution. In a similar vein, Yue, *et al.* [18] employed an atomic force microscope tip to conduct near field heating and thermal probing at sub-10 nm resolution. The Raman laser acted as both the heating source and temperature probe.

To precisely determine the temperature in the previously mentioned investigations of interface energy coupling, additional calibration was needed to build the relation between peak position, linewidth, intensity and temperature. Also precise knowledge of the amount of absorbed laser energy was needed for calculation of the temperature rise. Besides, other effects induced by temperature rise, like microstage shift, stress build-up in the sample holder due to extended heating, and the resulting out-of-focus effect, would all contribute to large measurement errors. The microstage shift and the out-of-focus effect induced the same trends of change in peak position, linewidth and intensity as those induced by temperature rise. They were rigorously treated and carefully removed in previous works [17, 19]. The stress effect could be de-conjugated from the difference between changes in linewidth and peak position.

It is critical to develop a method to eliminate the aforementioned disadvantages, but still take advantage of the Raman thermometry's unique features: high spatial resolution and the capability of distinguishing temperatures of materials in immediate contact. In this work, we will develop a new Raman technology to probe the temperature evolution of a sample under well-defined heating, and to determine the sample's thermal diffusivity. The new Raman technology is inspired by the transient electro-thermal (TET) technique that was developed in our lab for effective thermal characterization of one-dimensional solid materials [20]. The

#234498 - $15.00 USD Received 11 Feb 2015; revised 7 Apr 2015; accepted 8 Apr 2015; published 10 Apr 2015
© 2015 OSA

thermal diffusivity of various solid materials has been successfully and precisely determined by this technique [21–23]. In the TET technique, the sample is suspended between two electrodes where a step electrical current is applied. The sample's temperature evolution is obtained by probing the small temperature-induced resistance change. This technique is applicable for both electrical conductive and nonconductive materials. For nonconductive samples, a thin metallic coating is needed to make the sample electrically conductive and also to give a suitable resistance for Joule heating. The TET technique relies on electric connection and cannot be applied to the study of interfaces. Although Raman thermometry has unprecedented selective temperature measurement capacity and a very high spatial resolution, normal Raman technology is not able to probe transient temperature variations to achieve the same capacity of the TET technique.

In this work, a brand-new and compelling transient thermal probing and characterization technology is developed based on Raman thermometry and our TET concept: time-domain differential Raman (TD Raman). This new technique overcomes the drawbacks of other techniques listed above and is able to accurately measure the thermal diffusivity of materials. The potential application of this technique is demonstrated by measuring the thermal diffusivity of a microscale Si cantilever. Physical and mathematical models are developed to relate the measured Raman spectrum to the temperature evolution of the sample, and use this information to determine the sample's thermal diffusivity.

2. Time-domain differential Raman: physics and experimental setup

2.1 Concept and physics of TD Raman

To achieve well-defined heating and transient thermal probing, a single, modulated laser beam is used for both material heating and Raman excitation/thermal probing. Figure 1(a) shows the concept of the technique. In Case 1, the modulated laser cycle is designed to consist of an excitation period (t_e) followed by a thermal relaxation period (t_r). During the excitation period, the temperature of the sample rises due to continued laser heating. Raman scattering is also excited and collected during this period. Along with the rising temperature, the instantaneous Raman spectrum varies: the Raman peak intensity (I) decreases, the wavenumber (ω) softens and the linewidth (Γ) broadens. The schematic of Raman spectrum's properties variations is shown in Case 1 in Fig. 1(a). During the relaxation period the laser is switched off and the sample will cool down due to thermal dissipation to the heat sink or supporting structure. As the laser is off, neither is Raman scattering excited nor collected in this period. The thermal relaxation period t_r is long enough to allow the sample to completely cool down before the next excitation cycle starts. In one entire cycle, the excited Raman scattering signals are collected and accumulated over the whole excitation period t_e. Since one heating period is too short for Raman signal collection, multiple heating/cooling cycles are used in spectrum acquisition to ensure a sufficiently high Raman peak. Based on the number of heating/probing cycles in the measurement, the Raman signal of a single heating period can be simply obtained. The Raman spectrum in Fig. 1(b) shows the temporally accumulative Raman spectrum for this case.

After the first heating and thermal probing case is studied, we design a second modulated laser heating/probing case (Case 2). As illustrated in Fig. 1(a), the excitation period is a little longer than Case 1 by Δt_e, but the relaxation period is the same as Case 1. Thus, the entire cycle is extended by Δt_e while the frequency is decreased. The temperature increases further in the extended heating time (Δt_e), and the instantaneous I, ω, and Γ vary with increasing temperature. The changing rates are slower for the temperature and the Raman properties in the extended time than at the end of the laser pulse in Case 1.

#234498 - $15.00 USD Received 11 Feb 2015; revised 7 Apr 2015; accepted 8 Apr 2015; published 10 Apr 2015
© 2015 OSA

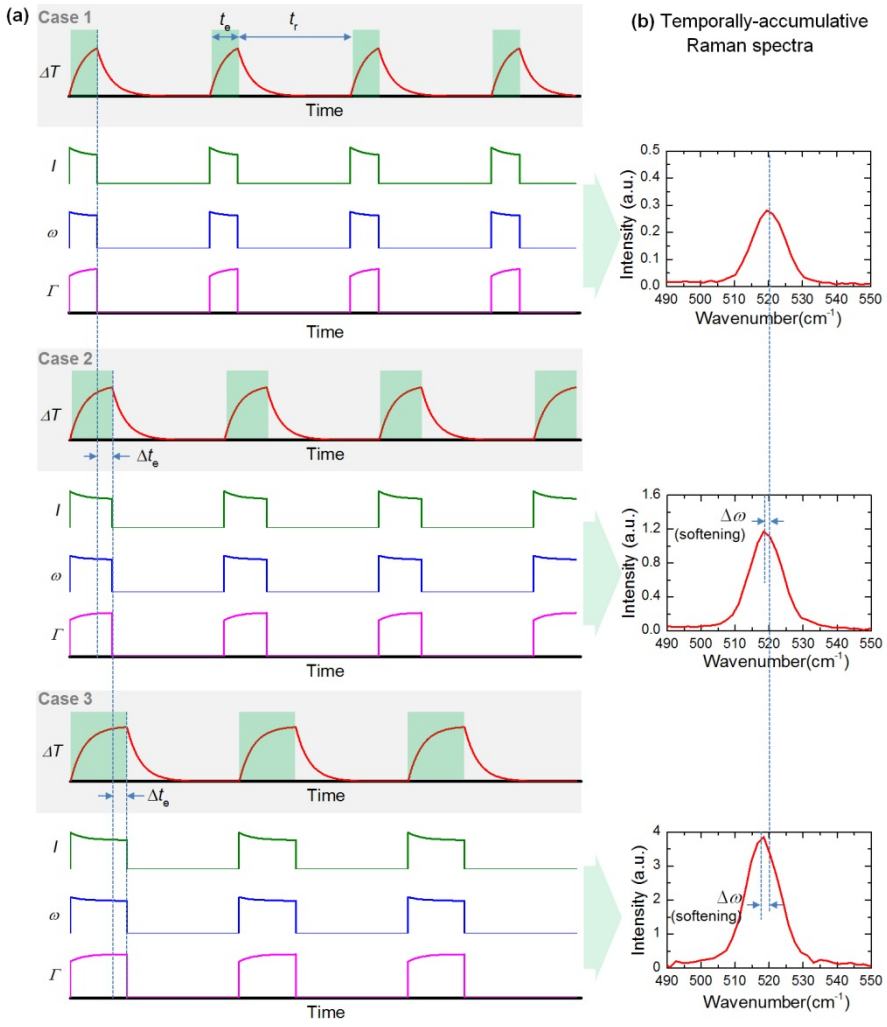

Fig. 1. (a) Timing profiles of the laser pulse and the temperature evolution, and instant changes of Raman peak intensity (I), peak shift (ω) and linewidth (Γ). Along with the heating, the temperature in the sample increases, and then the Raman peak intensity decreases, the wavenumber softens and linewidth broadens. In TD Raman, the laser heating time is increased a little bit (Δt_e) each time from Case 1 to Case 3. Therefore, the temperature of the heated region will experience more increase (before reaching the steady state) from Case 1 to Case 3. This extended temperature rise will give rise to a slight change in the Raman spectrum collected during the heating period. (b) The corresponding temporally accumulative Raman spectra of one cycle in three cases. Slight Raman peak softening due to the increased differential heating time is marked in the figure. The peak intensity increases largely because of the longer excitation period. The heating induced intensity decrease is less obvious in these spectra, but is visible via further peak analysis.

The collected temporally accumulative Raman spectrum [shown on the right in Fig. 1(b)] will differ from the Raman spectrum of Case 1 because of Δt_e. First, it will have a higher intensity due to the increased excitation time, because more scattered photons are sent to the spectrometer during this period. However, this intensity differential is not proportional to Δt_e. As shown in Fig. 1(a), since the excitation time is longer, the sample will have a greater temperature rise (if the steady state is not reached yet), resulting in a small reduction in the intensity increase. Second, since the collected Raman spectrum reflects the temperature information in the entire excitation cycle, the Raman spectrum with an extended excitation

#234498 - $15.00 USD Received 11 Feb 2015; revised 7 Apr 2015; accepted 8 Apr 2015; published 10 Apr 2015
© 2015 OSA

time will have Raman peak position softening due to the further temperature increase during Δt_e. In Fig. 1(b), this slight wavenumber softening is marked. Finally, the Raman spectrum in the new excitation case should have a broadened linewidth, since the sample has a higher average temperature during the excitation than in Case 1.

After the second excitation/probing case study is done, the excitation time of the laser is extended again while the thermal relaxation time is kept the same (Case 3). The instantaneous ΔT, I, ω, and Γ are shown in Case 3 in Fig. 1(a). The variations of ΔT, I, ω, and Γ are even smaller than those in Case 2. The frequency will then be even lower. The sample is heated, and the accumulated Raman spectrum is collected to reflect the temperature history over the excitation period. As we can see, with the increase of the excitation period by Δt_e in each case, the corresponding Raman spectrum will have a small change (differential). This change is related to the temperature rise of the sample induced by Δt_e. It can be used with further physical data handling to capture the realistic temperature evolution of the sample and to determine the thermal diffusivity of the sample.

It is better to construct a physical model for describing the normalized temperature evolution in a specific sample. Differing from other studies, the measured wavenumber, linewidth, and intensity in our work reflect an accumulative quantity of temperature variation during the pulse domain, but is not the time average. Variations in wavenumber, linewidth, and intensity against t_e are complexly related to the temperature increase. Rather, a precise physical model is needed to extract the temperature variation. With the correlation between variations of the Raman spectra and the normalized temperature rise, we can fit the normalized change of some properties of the Raman peak to determine the sample's thermal diffusivity.

2.2 Experiment design

The TD Raman idea is realized by integrating a square-wave-modulated diode laser into a commercial confocal Raman spectrometer. A continuous wave single longitudinal mode laser (MSL-III-532-AOM-150mW, Ultralaser, Inc.) is modulated with a function generator (DS345) to output variable duty cycle pulses. The laser is reflected by several mirrors to be integrated into the original optical path of a commercial confocal Raman system (Voyage, B&W Tek, Inc. and Olympus BX51). This laser is then focused on the sample surface with an objective lens and acts as both the heating and Raman excitation source. When the pulse is on, the laser heats the sample and induces a temperature rise of the sample surface. The Raman scattering signal collected simultaneously during this period contains temperature and thermal stress information. It is collected by the same objective lens in back scattering mode and sent to the Raman spectrometer. A beam splitter and a notch filter are placed in front of the spectrometer to filter out reflected the excitation light. Acquisition of the Raman spectrum is accomplished by using commercial software in a computer.

3. Si cantilever measurement: Raman spectrum variation against t_e

A carefully designed experiment for time-domain thermal probing and thermal characterization is conducted on a tipless silicon AFM cantilever (AppNano, Ltd.) in the open air at room temperature (293 K). The optical image of the tipless cantilever [Fig. 2(a)] shows that the tip is about 450.35 μm long, 49 μm wide and 2.5 μm thick. The tip end is a triangle with a height of 22.95 μm. The laser is focused on the tip end of the cantilever with a 4 × objective lens. The laser spot size is 31.4 × 65.3 μm^2 at the focal level. The long axis of the laser spot is perpendicular to the cantilever and the short axis is parallel to it in the horizontal plane (Fig. 2(b)). 7.9 mW laser energy is carefully selected to heat the cantilever, while the range of the temperature rise is still small enough that the Raman spectrum properties are considered linearly correlated with temperature rise. Also, the small thermal energy input would not induce damage on the cantilever. It is proved by a repeated measurement on the same irradiated spot that no obvious change in the spectrum was observed. To simplify the

#234498 - $15.00 USD Received 11 Feb 2015; revised 7 Apr 2015; accepted 8 Apr 2015; published 10 Apr 2015
© 2015 OSA

evaluation of the temperature-induced change of the Raman signals, an approximation of a square tip end is applied to our physical model as shown in Fig. 2(b). The total length L used in the physical model is 438.9 μm and the length of irradiation area l_e is 19.9 μm.

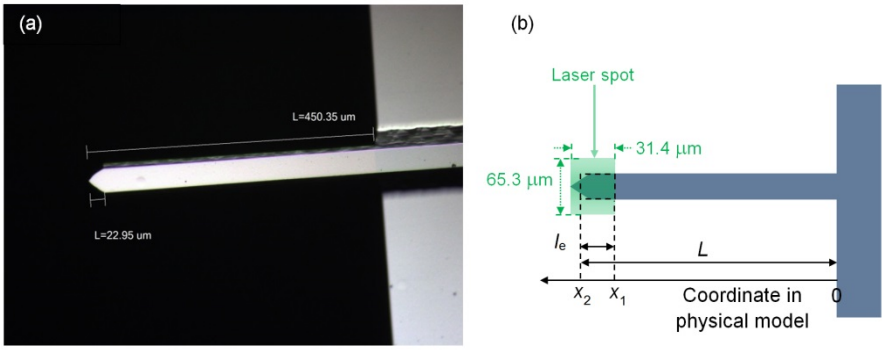

Fig. 2. (a) The optical microscope view of the tipless Si cantilever. It is 450.35 μm long and 49 μm wide. The tip has a height of 22.95 μm. (b) Schematic of laser spot position on the cantilever tip end. The effective heating region is marked with x_1 and x_2 on the x coordinate in the physical model. l_e (= x_2 - x_1) is 19.9 μm indicating the effective length of the heating region on the cantilever. L is the total effective length (438.9 μm) used for the cantilever in the physical model.

The characteristic heat transfer time of this cantilever in the length direction is estimated as $0.81L^2/\alpha$ [20]. With bulk Si's reference thermal diffusivity α of 8.92×10^{-5} m^2/s at 300 K [24], this characteristic time is around 1.75 ms. The relaxation time (t_r) is fixed as 10 ms during which the cantilever can definitely relax to the room temperature and the cumulative thermal effect in the cantilever can be completely eliminated. Meanwhile, the length of the excitation period is adjusted from 20 μs to 30 ms to cover the whole transient range of temperature rise from room temperature to the steady state temperature. The increment of t_e in the experiment is varied in order to best reflect the change of the Raman spectrum against the heating time. The integration time for an individual spectrum is also selected to cover many pulse cycles and obtain a strong Raman signal for analysis. Differences in collecting cycles and time will be normalized later in the data processing.

Eight selected experimental Raman spectra of the Si peak are normalized to represent the signal for one excitation cycle [Fig. 3(a)]. With increased excitation time, the Si Raman peak shifts to a smaller wavenumber (softening) and broadens a little bit. This is due to an increase in temperature with increasing t_e. Also with increased t_e, the Raman intensity becomes larger because the excitation time is longer. Figures 3(b)-3(d) show variations of the peak intensity (E_ω) and the time-averaged one ($E_\omega^* = E_\omega/t_e$), linewidth ($\Gamma$), and wavenumber ($\omega$) against the excitation time. The subscript "ω" means that the maximum intensity is from the peak center wavenumber ω, which softens along with the increase of the heating time. For the Raman peak intensity, E_ω increases with increased t_e, since when t_e is longer, the Raman excitation is longer and a stronger signal is expected. Theoretically, if there is no temperature rise (heating), the Raman peak intensity should increase linearly with t_e. However, as seen in Fig. 3(b), in the beginning, the Raman intensity increases fast. This rate slowes down and finally reaches a relatively constant rate (slope). The observed decrease in $\partial E_\omega / \partial t_e$ is related to both the laser heating time and the temperature rise. Our recent studies show that when the temperature increases, the Raman intensity will decrease [13–15]. When t_e gets longer, the cantilever will reach the steady state (no further increase in the temperature), and the Raman intensity will increase with t_e linearly. The normalized Raman peak intensity E_ω^* is calculated as E_ω/t_e. It eliminates the effect of the varied t_e and shows a decreasing trend against the excitation time. The decreasing rate is fast at the beginning while the average temperature

#234498 - $15.00 USD Received 11 Feb 2015; revised 7 Apr 2015; accepted 8 Apr 2015; published 10 Apr 2015
© 2015 OSA

rises more quickly. As the cantilever is approaching the steady state (longer t_e), the average temperature rise gradually becomes a constant and so as E_ω^*.

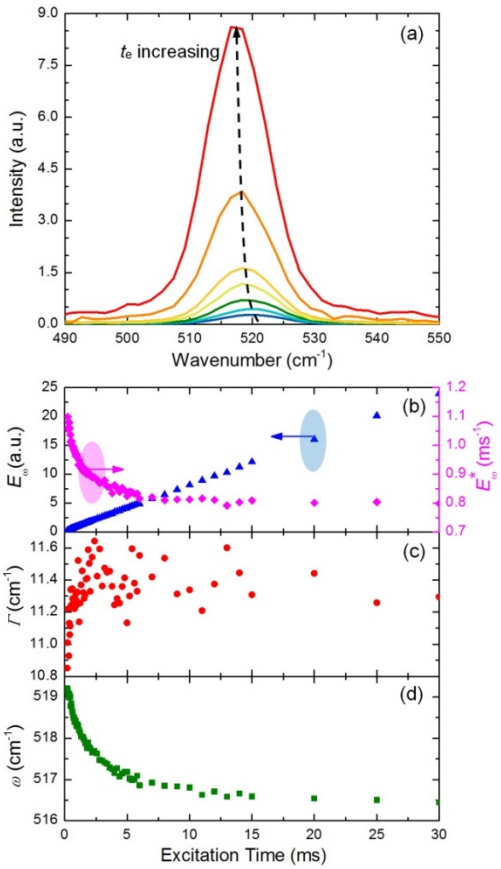

Fig. 3. The evolution of the Si Raman peak against the increase of excitation/heating duty in the experiment. (a) Spectra per cycle under different excitation time of t_e: 0.24 ms, 0.4 ms, 0.68 ms, 1.16 ms, 1.72 ms, 4.2 ms, and 10 ms. As the excitation/heating time becomes longer, the Raman peak in one cycle increases and softens to the left. (b) Raman emission E_ω (to the left y axis) increase against t_e, but the rate $\partial E_\omega/\partial t_e$ declines quickly at the beginning and then slows down to a constant. The normalized Raman emission E_ω^* (to the right y axis) decreases to a steady state value as t_e become longer. E_ω^* directly illustrates that the Raman emission per unit time decreases against the heating time. (c) Raman linewidth variation against the excitation time. Although an increasing trend is observed for the linewidth against increased excitation time, large noises are observed in linewidth data due to the less sensivity of linewidth to temperature variation. So this data is less applicable for thermal diffusivity determination. (d) A clear decline in the wavenumber against t_e makes wavenumber ω a good property for detemining α of the cantilever.

For the linewidth [Fig. 3(c)], although an increasing trend is observed against increased excitation time, the signal to noise ratio (SNR) is small due to the small variation of linewidth with temperature. For the wavenumber (Fig. 3(d)), it experiences quick decay because of the fast temperature increase at the beginning of the laser heating. During this period, the increasing rate of temperature is mainly determined by the heating rate since the heat conduction is weak. Along with the heating (longer t_e), thermal transport to the heat sink (the chip) becomes more important while the laser heating rate remains the same. Thus the heat

#234498 - $15.00 USD Received 11 Feb 2015; revised 7 Apr 2015; accepted 8 Apr 2015; published 10 Apr 2015
© 2015 OSA

dissipation slows down the rate of the temperature rise in the sample. As a result, the wavenumber changes slower at the longer t_e than it did around the beginning. The wavenumber shown in Fig. 3(d) is Raman intensity weighted over the time: 0 ~t_e. Therefore its rate of change against t_e is slower than the real temperature changing rate. These changes are tightly associated with the temperature rise in the cantilever.

As we stated above, the measured Raman peak intensity, linewidth, and wavenumber is an intensity-weighted average over 0 ~t_e, and could not reflect the instantaneous temperature variation against time. To utilize the Raman spectrum to determine the thermal diffusivity, physical model development is necessary to describe the temperature evolution of the laser heated region, to relate the measured Raman spectrum to the temperature evolution with consideration of temperature dependent Raman intensity, and to fit the reduced Raman spectrum variation against t_e.

4. Physical model for temperature evolution

The characteristic thermal diffusion time of a material is proportional to l^2, where l is the thermal diffusion length. The cantilever is 2.5 μm thick and 450.35 μm long. The characteristic thermal diffusion time in the thickness direction (τ_1) of the cantilever is negligible in comparison with the time (τ_2) taken by the whole cantilever to reach the thermal steady state ($\tau_1 \sim 3 \times 10^{-5}\tau_2$) in the length direction. Although the cantilever is heated at the end from the top surface, it is physically reasonable to assume that the temperature field is uniform across the cross-section. This 1D approximation (along the length direction) is applicable for evaluating the heat transport from the tip end of the cantilever to the chip. Neglecting radiation and convection (discussed later), the heat transport in the cantilever along the length direction can be expressed as:

$$\rho c_p \frac{\partial \theta}{\partial t} = k \frac{\partial^2 \theta}{\partial x^2} + \dot{g}, \tag{1}$$

where $\dot{g}$ is the heating induced by the laser pulse at the tip end. The x coordinate is shown in Fig. 2(b). ρ, c_p, and k are the density, specific heat, and thermal conductivity, respectively. An adiabatic boundary condition is imposed on the tip end, and the other end is treated as a heat sink with a constant temperature of 293 K. θ is the temperature rise as a result of pulsed laser heating. At the beginning, θ is 0 K in the whole cantilever. The Green's function method is employed to solve Eq. (1):

$$G_{X11}(x,t|x',\tau) = \frac{2}{L}\sum_{m=1}^{\infty} e^{-m^2\pi^2\alpha(t-\tau)/L^2} \times \sin(m\pi\frac{x}{L})\sin(m\pi\frac{x'}{L}), \tag{2}$$

$\alpha = k/\rho c_p$ is thermal diffusivity. The temperature rise has the expression of:

$$\theta(x,t) = \frac{\alpha}{k}\int_{\tau=0}^{t}\int_{x'=x_1}^{x_2} G_{X11}(x,t|x',\tau)\dot{g}dx'd\tau. \tag{3}$$

Since the excited Raman signals are collected at the tip end, a spatially averaged temperature in the heated region is used to describe the temperature evolution probed by the Raman spectrum. This is physically reasonable since the heated region is very small, and the temperature distribution over it is very uniform. In the 1D model, x_1 = 427.4 μm and x_2 = 438.9 μm are the coordinates of the effective heated region on the tip surface. The origin is located at the conjunction point of the cantilever and the chip shown in Fig. 2(b). The solution for the spatially averaged temperature rise at one instant is:

$$\bar{\theta}(t) = \frac{2\dot{g}L^3}{(x_2-x_1)k}\sum_{m=1}^{\infty}\frac{1}{m^4\pi^4}(1-e^{-\frac{m^2\pi^2\alpha}{L^2}t})(\cos\frac{m\pi}{L}x_1 - \cos\frac{m\pi}{L}x_2)^2. \tag{4}$$

#234498 - $15.00 USD Received 11 Feb 2015; revised 7 Apr 2015; accepted 8 Apr 2015; published 10 Apr 2015
© 2015 OSA

At steady state ($t \to \infty$), the final temperature rise $\bar{\theta}_{ss}$ has the expression of

$$\bar{\theta}_{ss} = \frac{2\dot{g}L^3}{(x_2 - x_1)k} \sum_{m=1}^{\infty} \frac{1}{m^4\pi^4} (\cos\frac{m\pi}{L}x_1 - \cos\frac{m\pi}{L}x_2)^2. \tag{5}$$

The normalized temperature rise $\bar{\theta}^*$ with respect to $\bar{\theta}_{ss}$ is

$$\bar{\theta}^* = \bar{\theta} / \bar{\theta}_{ss} = \frac{\sum_{m=1}^{\infty} \frac{1}{m^4\pi^4} (1 - e^{-\frac{m^2\pi^2\alpha}{L^2}t}) (\cos\frac{m\pi}{L}x_1 - \cos\frac{m\pi}{L}x_2)^2}{\sum_{m=1}^{\infty} \frac{1}{m^4\pi^4} (\cos\frac{m\pi}{L}x_1 - \cos\frac{m\pi}{L}x_2)^2}. \tag{6}$$

Considering the linear correlations between temperature rise and variations in Raman peak intensity, wavenumber and linewidth in a small range of temperature variation, the change of the Raman spectrum in the experiment can be evaluated by considering the evolution of $\bar{\theta}^*$.

5. Physical model and numerical reconstruction of Raman spectrum

At any instant t during the excitation cycle, 0~t_e, the Raman signal emitting rate can be expressed as [assuming the Raman peak takes the Gaussian distribution, which usually holds up]

$$I(\omega) = A_t \exp[-\frac{4\ln 2 \cdot (\omega - \omega_t)^2}{\Gamma_t^2}]. \tag{7}$$

$I(\omega)$ is the Raman emission rate at frequency ω, and A_t is the rate at the Raman peak location ω_t. Γ_t is the Raman linewidth. Note that A_t, ω_t and Γ_t all depend on temperature, so they change with time t during the excitation cycle because temperature changes with t. The calibration in previous studies [13–15] reveals the linear temperature-dependent feature of Si Raman peak properties over a temperature range from 20 to 200 °C. Thus, in this work, this feature can be expressed as $A_t = A_0(1 - A\bar{\theta}^*)$, $\omega_t = \omega_0 - B\bar{\theta}^*$, and $\Gamma_t = \Gamma_0 + C\bar{\theta}^*$, where A_0, ω_0. Γ_0 are the corresponding Raman properties at the beginning of laser heating (no temperature rise yet). Constants A, B, and C are the changing rate of the Raman intensity, peak location, and linewidth against the normalized temperature. The accumulative Raman emission (at wavenumber ω) for the entire excitation cycle from 0 to t_e can be obtained by integrating $I(\omega)$ over time as

$$E_\omega(\omega, t_e) = A_0 \int_0^{t_e} (1 - A\bar{\theta}^*) \exp\left[-\frac{4\ln 2 \cdot (\omega - \omega_0 + B\bar{\theta}^*)^2}{(\Gamma_0 + C\bar{\theta}^*)^2} \right] dt. \tag{8}$$

In Eq. (6), the variable t and the parameter α can be grouped together as the Fourier number Fo ($Fo = \alpha t/L^2$). Thus, from Eqs. (6) and (8), we can tell that both temperature rise and Raman intensity depend on Fo. Substituting Fo into Eq. (8), the correlation between the excitation time and Raman spectrum has the expression of

$$E_\omega(\omega, Fo_e) = A_0 \int_0^{Fo_e} (1 - A\bar{\theta}^*) \exp\left[-\frac{4\ln 2 \cdot (\omega - \omega_0 + B\bar{\theta}^*)^2}{(\Gamma_0 + C\bar{\theta}^*)^2} \right] dFo, \tag{9}$$

where $Fo_e = \alpha t_e/L^2$. For the Raman peak intensity variation against t_e as shown in Fig. 3(b), its increase against the excitation time carries the integration time's effect. Instead of using the cumulative Raman emission for the entire excitation cycle, we use the time average for

#234498 - $15.00 USD Received 11 Feb 2015; revised 7 Apr 2015; accepted 8 Apr 2015; published 10 Apr 2015
© 2015 OSA

analysis. This is done by simply dividing the left term in Eq. (9) by Fo_e. The expression of this normalized intensity is

$$E_\omega^*(\omega, Fo_e) = \frac{A_0}{Fo_e}\int_0^{Fo_e}(1-A\bar{\theta}^*)\exp\left[-\frac{4\ln 2\cdot(\omega-\omega_0+B\bar{\theta}^*)^2}{(\Gamma_0+C\bar{\theta}^*)}\right]dFo, \qquad (10)$$

where $E_\omega^*(\omega, Fo_e) = E_\omega(\omega, Fo_e)/Fo_e$. The values of constants A_0, ω_0, Γ_0, A, B, and C in Eq. (10), can be extracted from the normalized peak intensity, wavenumber, and linewidth variation against t_e (shown in Fig. 3) by evaluating the limit at $t_e \to 0$ and $t_e \to \infty$. However, because even the Raman spectrum with the shortest t_e inevitably has some heating effect, the extracted thermal properties and Raman scaling constants will deviate from the actual values. Thus these constants are refined to better approach the actual values which are then used for fitting experimental data. The refining process will be detailed in Section 6. They are finally determined as $A = 0.31$, $\omega_0 = 507.22$ cm^{-1}, $B = 3.7$ cm^{-1}, $\Gamma_0 = 11.06$ cm^{-1}, and $C = 0.34$ cm^{-1}. Constant A_0 is less important to us for we are only interested in the relative Raman intensity variation.

Based on Eq. (9), the reconstructed Raman spectrum per cycle at different Fo_e is shown in Fig. 4(a). It is observed when Fo_e increases, the Raman peak shifts to the left (softening), the linewidth slightly broadens, and the Raman peak intensity increases largely as the excitation/collecting time becomes longer. Figures 4(b) and 4(c) show how the normalized Raman intensity and wavenumber vary with Fo_e. The normalized Raman intensity E_ω^* decreases with increased Fo_e. This is because when Fo_e is larger, the average temperature of the sample during that period is higher. As a result, the average Raman signal becomes smaller. Also we fit the reconstructed Raman peaks and determine their peak intensity and peak location at different Fo_e. The reconstructed E_ω^* and ω show similar trends to the experimental results shown in Figs. 3(b) (the right y axis) and 3(d). However, how fast or slow they change with time depends on the thermal diffusivity of the sample. Fo_e here only gives a non-dimensionalized time.

6. Thermal diffusivity determination based on ω and E^*

Although the Raman linewidth is directly related to temperature, the SNR for the linewidth measurement is too small to precisely determine the thermal diffusivity of the Si cantilever. Instead, we use the variations of the normalized Raman intensity and the peak shift for the thermal diffusivity determination. In the fitting process, the initial values of constants A_0, ω_0, Γ_0, A, B, and C are directly read from the experimental data and substituted into Eq. (10). As mentioned above, some heating effect inevitably exists in the initial state of the experiment as we cannot make t_e extremely short while collecting sufficient Raman signal. The extracted initial values of those constants from Fig. 3(b) will deviate from their real values. Fine adjustment of them is then performed in determining the cantilever's thermal diffusivity. If an extremely short t_e could be realized, the heating effect could be safely neglected and the A, B, and ω_0 can thus be directly measured. The improvement of TD Raman technology with respect to shorten the excitation time will be pursued in near future.

#234498 - $15.00 USD Received 11 Feb 2015; revised 7 Apr 2015; accepted 8 Apr 2015; published 10 Apr 2015
© 2015 OSA

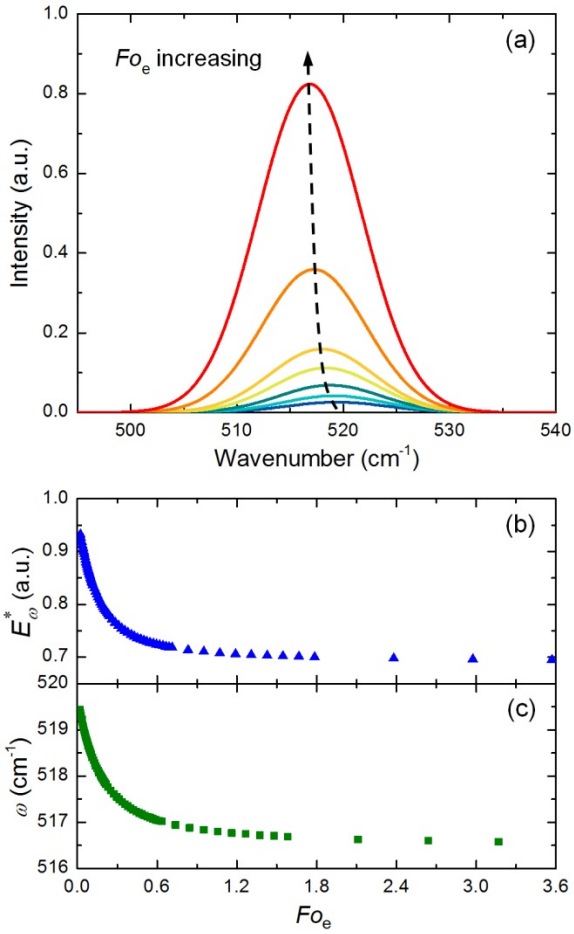

Fig. 4. (a) The evolution of the reconstructed Si Raman spectrum per cycle with the numerical method against the increase of Fourier number Fo_e (t_e): 0.028, 0.047, 0.079, 0.14, 0.20, 0.49, and 1.17. The Raman peak in one cycle increases and softens to the left against the increased Fo_e. This echoes the one in Fig. 3(a). (b) The decreasing trends of the normalized Raman intensity E^*_ω and (c) the Raman shift ω against the Fourier number Fo_e well agree with the trends in the experiment.

In the fitting process, ω_0, A and B are scanned over a specified reasonable range. For each combination of ω_0, A and B, based on Eq. (10), we reconstruct the Raman spectrum at different Fo_e, and obtain curves like those shown in Figs. 4(b) and 4(c). Note these curves do not have the time information yet. For each thermal diffusivity, the Fo_e can be converted to time, and the curves become time-related. Then these curves are compared with those experimental data in Figs. 3(b) and 3(d) using the least square method and obtain a deviation (σ: root mean square of differences) at the end of the comparison. A_0 is not needed as we are only interested in the relative Raman intensity variation. Then we scan the thermal diffusivity from 5.05×10^{-5} m^2/s to 12×10^{-5} m^2/s with an increment of 1% each step. The whole fitting process is run to find the smallest σ and returns the corresponding ω_0, A, and B, and α. Refining is also conducted on Γ_0 and C, but it is observed that the extracted Γ_0 and C is very close to their initial values due to temperature sensitivities. Thus their initial values read from Fig. 3(b) are directly used in the entire fitting process. The thermal diffusivity giving the best fit of the experimental data is taken as the property of the sample. The experimental data and

#234498 - $15.00 USD Received 11 Feb 2015; revised 7 Apr 2015; accepted 8 Apr 2015; published 10 Apr 2015
© 2015 OSA

best fitted curves for the normalized intensity and the wavenumber based on the Eq. (10) are shown in Figs. 5(a) and 5(b).

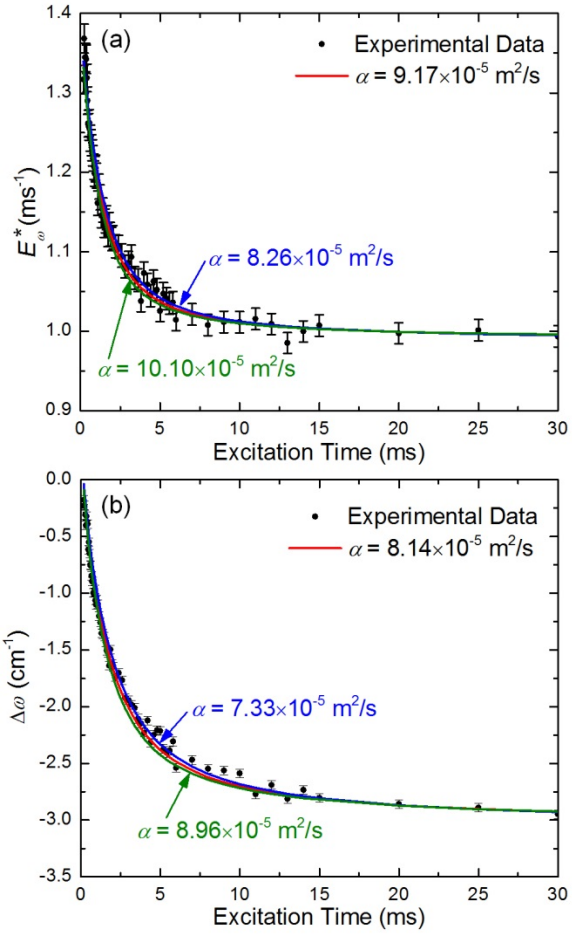

Fig. 5. (a) Variation of normalized intensity against the excitation time. It decreases as t_e is increasing to a steady state value. The red curve with $\alpha_{E^*_\omega}$ of 9.17 × 10^{-5} m^2/s best fits the experimental data based on the intensity method. (b) Wavenumber shift to the steady state against the excitation time. The best fitted curve with α_ω of 8.14 × 10^{-5} m^2/s is shown red. Error bars in both figures show the uncertainty in the measurement, and curves with 10% deviation in both thermal diffusivities are shown in blue and green. They show obvious difference from the best fitted results indicating the sensitivity of the normalized Raman intensity method and wavenumber shift method, respectively.

The normalized intensity decreases against the excitation time to the steady value. The best fitted curve with an $\alpha_{E^*_\omega}$ of 9.17 × 10^{-5} m^2/s follows the trend of the normalized intensity in the experiment well. The uncertainty of the normalized intensity in the peak analysis is indicated by the error bars in Fig. 5(a). To illustrate the sensitivity of the normalized Raman intensity method, two curves of ± 10% variations in $\alpha_{E^*_\omega}$ are plotted in blue and green in Fig. 5(a). Across the whole t_e span, a visible change is observed for these two curves compared with the best fitting results, indicating this method is sensitive to determine thermal diffusivity. Though these two curves of ± 10% variations in $\alpha_{E^*_\omega}$ could not cover all the measurement errors, they best limit the changing trend of the fitted curve to well follow the

#234498 - $15.00 USD Received 11 Feb 2015; revised 7 Apr 2015; accepted 8 Apr 2015; published 10 Apr 2015
© 2015 OSA

experiment result. The accurate changing trend is more important in our fitting process. Most experimental data fall in between the ± 10% curves even though the error level is much broader. Figure 5(b) shows the change in wavenumber shift against t_e and error bars show the wave number uncertainty in peak fitting. The curve with an α_ω of 8.14×10^{-5} m^2/s gives the best fit (red), and the other two curves, varying 10% in α_ω, are plotted for showing the sensitivity of the wavenumber fitting method.

7. Physical analysis and experimental uncertainty evaluation

To evaluate the measured thermal diffusivity, we first estimate the temperature rise in the Si cantilever's tip end with the physical mode shown in Fig. 2(b). The final temperature rise ΔT in the irradiated area can be calculated with the equation $q = kA_{\text{cross}}\Delta T_{\text{ss,tip}} / L$. q is the absorbed laser power which is the product of the incident laser power on the surface of the tip end and the absorbance of single crystal Si (0.626 at 532 nm). k is the thermal conductivity of bulk Si (148 W/m·K) at 300 K, and A_{cross} is the cross-section area of the cantilever. The steady state temperature rise ($\Delta T_{\text{ss,tip}}$) is determined to be 57 K at the tip end of the Si cantilever. The thermal diffusivity α in the physical model in Eq. (4) reflects a spatial-average value for describing the temperature evolution in the whole cantilever. The temperature linearly decreases from the tip end to the chip, so the spatial-average temperature is half of $\Delta T_{\text{ss,tip}}$ at the steady state.

As discussed in Section 3, time averaging is performed in constructing the correlation between the temperature rise and the peak profile. Actually, the obtained raw Si Raman peak is an accumulated signal over the excitation period. The normalization of the intensity excludes the varied excitation time and averages the peak profile. The thermal diffusivity determined by the physical model fitting contains another average in the time domain. For, $\Delta T_{\text{ss,tip}}/2$ is a sound approximate of the spatial-average temperature rise at the steady state, the final average temperature rise that determines the fitted thermal diffusivity in the cantilever is about $\Delta T_{\text{ss,tip}}/4$. This characteristic temperature rise $\bar{\theta}_{th}$ is about 14 K. Our TD Raman experiment is carried out at room temperature (293 K), so the spatially-and-temporally-averaged temperature of the Si cantilever is 307 K. The corresponding reference thermal diffusivity α_{ref} of single crystal silicon is 8.66×10^{-5} m^2/s at this temperature. In fact, considering the thickness of the cantilever, the temperature distribution could be uneven from the upper part to the bottom of the cantilever. The real average temperature rise will be even lower than 14 K and then the thermal diffusivity will be a little larger than 8.66×10^{-5} m^2/s.

Due to the extremely small size and the delicate feature of the cantilever, a regular thermocouple could not be applied for real-temperature measurement. To compare with the above analysis, the temperature rise is examined from the experimental variations in linewidth, normalized intensity, and wavenumber of the Si Raman peak. Among them, the temperature change based on linewidth is the most straightforward to analyze. However the small SNR associated with the linewidth measurement makes it difficult for accurate fitting. The linewidth of the Si peak increases by about 0.34 cm^{-1} in Fig. 3(c) from the initial state to the steady state in the experiment. So the total temperature rise at the cantilever end is 38 K and the average temperature $\bar{\theta}_{\Gamma}$ is 9.5 K, with the temperature coefficient of 0.009 cm^{-1}/K calibrated in our previous work [14]. It is a little lower than, but very close to $\bar{\theta}_{th}$. The Si Raman spectrum with the shortest excitation period is taken as the initial state to evaluate the temperature rise. This experimental initial state still has a little temperature rise, while the real initial state should be extracted from the Si Raman peak without heating effect. Thus, the linewidth of the real initial state should be narrower. It is reasonable that $\bar{\theta}_{\Gamma}$ is a little lower than $\bar{\theta}_{th}$.

#234498 - $15.00 USD Received 11 Feb 2015; revised 7 Apr 2015; accepted 8 Apr 2015; published 10 Apr 2015
© 2015 OSA

In the intensity method, we use the normalized intensity ratio of the steady state to the initial state to estimate the total temperature rise. This ratio is 74.6% from Fig. 5(a) and the determined temperature rise is about 108.8 K based on the temperature coefficient of 0.0024 K^{-1} [14]. Analogous to $\overline{\theta}_{\Gamma}$, averaged temperature $\overline{\theta}_{E_\omega^*}$ will be 27.2 K, which is higher than $\overline{\theta}_{th}$. Several factors could account for this deviation. One is the unevenly distributed temperature-induced thermal stress in the cantilever. This thermal stress is high in the upper irradiated area of the cantilever. The cantilever's deflection is the factor resulting from the uneven thermal stress and expansion. It will cause an out-of-focus effect during the Raman spectra acquisition, though the deflection is invisible to naked eyes under the 4 × objective lens. These thermal stress induced effects will lead to the reduction in the Si Raman intensity at the steady state and increase $\overline{\theta}_{E_\omega^*}$.

Another possible reason is the inaccuracy of the initial state value in the experiment. On one hand, large noises are observed at the beginning of the experimental data in Fig. 5(a), which will obscure the real initial intensity. On the other hand, when the excitation period is short, a long integration time is necessary to obtain a strong signal: about 15 minutes signal acquisition is needed for a sound spectrum when the excitation time is 20 μs. This may cause an additional out-of-focus effect due to the backlash of the sample stage and vibration in the environment. Moreover, the deficiency in the square pulse of the modulated laser will lower the temperature rise of the shortest excitation time. The modulated laser has a rising time of 0.13 μs. Though the total amount of thermal input is fixed, the heating rate is slower at the beginning of the excitation period than the rest and the temperature of the cantilever correspondingly rises slower in the beginning. Due to the fact that Raman intensity is highly sensitive to temperature, the instant intensity in the pulse rising time will increase the average intensity of the entire excitation period. When t_e is as short as 20 μs, the rising time will result in ~1% increase in the average temperature and the Raman intensity. When t_e is longer in our experiment, the effect of the rising time becomes negligible. Therefore, the total variation in E_ω^* is, to some extent, increased and so as $\overline{\theta}_{E_\omega^*}$. But the increase in ΔE_ω^* will "stretch" the real curve and accelerate the changing rate of the curve, and thus cause the 5.9% deviation in the measured $\alpha_{E_\omega^*}$ of 9.17 × 10^{-5} m^2/s from the reference thermal diffusivity of 8.66 × 10^{-5} m^2/s.

In Fig. 5(b), the total wavenumber shift is about 2.8 cm^{-1}. It is several times larger than the broadening in the linewidth, though the temperature coefficient for the wavenumber is just twice that for the linewidth. The total shift of wavenumber is a combined result from not only the sole temperature rise but also the thermal stress and other factors in the cantilever. We could not directly evaluate $\overline{\theta}_{\omega}$, but our model is still applicable for fitting the variation of the wavenumber shift. The stress and other possible factors could approximate to a first-order function of θ to simplify the fitting process. They are all included in constant B in α determination in Eq. (8). The best fitted result α_ω is 8.14 × 10^{-5} m^2/s. It is 5.8% lower than the reference value of 8.66 × 10^{-5} m^2/s.

The thermal radiation and convection effect in the determined thermal diffusivity of the cantilever can be evaluated with the equation of $(8\varepsilon\sigma T_0^3 + 4h)L^2 / (\rho c_p D\pi^2)$ [21, 25]. ρ, c_p, and ε, are density (2330 kg/m^3), specific heat (712 J/kg·K), and emissivity (< 0.1) of bulk Si at room temperature. h is the free convection coefficient, which is about 1~2 W/m^2·K at 300K. L and D are the length (438.9 μm) and the thickness (2.5 μm) of the Si cantilever. The thermal radiation and convection effect will give a negligible error of ~4.8 × 10^{-8} m^2/s in the determined thermal diffusivity.

#234498 - $15.00 USD Received 11 Feb 2015; revised 7 Apr 2015; accepted 8 Apr 2015; published 10 Apr 2015
© 2015 OSA

8. Thermal diffusivity determination based on total Raman emission

Raman peak intensity is a typical property representing the Raman scattering efficiency of a material. However, with the existence of the incident light broadening, heating effects, surface refraction and reflection, and detector efficiency, additional references and calibrations are needed if the intensity is used to analyze the Raman emission [26, 27]. Furthermore, in the numerical model, the Raman spectrum is a complex composition of the peak intensity, the wavenumber and the linewidth. Each property will affect the determination of the other two. It is also very time consuming to reconstruct spectra for all excitation duties in the experiment.

Instead of using the Raman peak intensity, the Raman peak area could be an alternative property to evaluate the total Raman emission over the whole peak range of wavenumber. In this section, we develop a simplified physical model on the basis of the total Raman emission to fit the thermal diffusivity of the Si cantilever. The Raman peak area is proportional to the product of the linewidth and the peak intensity in the Gaussian function. The Raman wavenumber shift does not affect the peak area evaluation. In experimental data processing, the normalization of the Raman peak area is first conducted to the excitation time. The normalized peak area indicates the average Raman emission per unit time in the excitation period. It is also related to the average temperature rise in the Si cantilever. The normalized total Raman emission, E^*, is simplified as:

$$E^* = \frac{A_0^{'}}{t_e}\int_0^{t_e}(1-A\overline{\theta}^*)(\Gamma_0 + C\overline{\theta}^*)dt, \tag{11}$$

$A_0^{'}$ is a multiple compensating for the difference in the peak area between the normalized experimental data and the average fitting result. It is determined by comparing experimental data with theoretical data at steady state. Similar to A_0, $A_0^{'}$ is less significant to us while the relative variation of the peak area is more useful. Constants Γ_0 and C are directly extracted from the linewidth variation of the experimental spectra, and take the values indicated above ($\Gamma_0 = 11.06$ cm^{-1} and $C = 0.34$ cm^{-1}).

A and C are the changing coefficients of the normalized peak intensity and linewidth against the normalized temperature rise. Based on the A value extracted from Fig. 3(b), refinement is also conducted together with the determination α in the peak area fitting process. A is varied from 0.1 to 0.4 with an increment of 1%. For each A, α is scanned from 3 × 10^{-5} m^2/s to 12 × 10^{-5} m^2/s. The best fitted values of A and α_{E^*} are 0.32 K^{-1} and 9.51 × 10^{-5} m^2/s, respectively, for constructing a theoretical curve that fits the experimental data best (Fig. 6). The value of A is very close to the one determined above based on the precise physical mode: 0.31 K^{-1}. In Fig. 6, error bars indicate the peak area measurement uncertainty and the blue and green curves with 10% deviation in α illustrate the sensitivity of the total Raman emission method.

Compared with the reference value in Section 6, α_{E^*} from the total Raman emission method has a 10% deviation from α_{ref}. α_{E^*} has a larger error than those from the intensity method and wavenumber method because it is the product of Raman intensity and linewidth. Errors of the normalized intensity and linewidth will be combined together during thermal diffusivity determination based on the peak area method. The advantage of the peak area fitting method (or total Raman emission method) is that it provides a quick way to determine the thermal diffusivity of a material. The peak area method utilizes the linewidth variation against the excitation time. No other information is needed for the Raman wavenumber and shift. Thus, it avoids the Raman spectrum re-construction, which is very time consuming.

#234498 - $15.00 USD Received 11 Feb 2015; revised 7 Apr 2015; accepted 8 Apr 2015; published 10 Apr 2015
© 2015 OSA

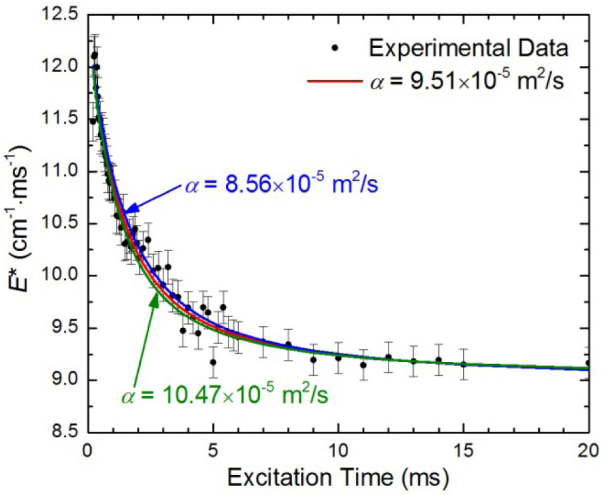

Fig. 6. The experimental data fitting based on the peak area with the best fitted curve with α_{E^*} = 9.51 × 10^{-5} m^2/s. The measurement uncertainty is shown using error bars. The sensitivity of the total Raman emission method to α is shown with α = 8.56 × 10^{-5} m^2/s and α = 10.47 × 10^{-5} m^2/s, respectively. A visible deviation is observed from the best fitted result when α changes with 10%.

9. Conclusion

In this work, a time-domain differential Raman technology was successfully developed for characterizing thermal transport in a tipless Si cantilever along the length direction. A physical model was first developed for describing the temperature evolution in the cantilever against the increased heating time. The variation of the Si Raman spectrum was also correlated with the normalized temperature rise through developing a precise physical model for Raman spectrum reconstruction. The thermal diffusivity of the cantilever was determined at 9.17 × 10^{-5}, 8.14 × 10^{-5}, and 9.51 × 10^{-5} m^2/s by fitting the variation of Raman peak intensity, wavenumber, and peak area against heating time. To evaluate this new technique, the real temperature rise (timely-and-spatially averaged for the thermal diffusivity) was calculated at 14 K. The corresponding reference thermal diffusivity α_{ref} is 8.66 × 10^{-5} m^2/s. All three determined results were very close to the reference value. The deviation was induced by the inaccurate definition of the initial state and the heat induced deflection and out-of-focus effect. The most important advantage of the TD Raman technique is that the specific temperature of the sample at any instant is not needed to study thermal transport. Only the normalized variation of the temperature rise is needed. Thus no calibration was conducted in this work. The normalized variation in the Raman intensity and wavenumber can be directly and accurately analyzed to determine the thermal diffusivity of the sample.

Acknowledgments

Support of this work by DOE (DENE0000671) is gratefully acknowledged. X.W and Y.Y also thank the support of National Natural Science Foundation of China (No. 51428603), and "Chutian" Scholar program of Hunan Province, China.

#234498 - $15.00 USD Received 11 Feb 2015; revised 7 Apr 2015; accepted 8 Apr 2015; published 10 Apr 2015
© 2015 OSA